Ultrafast Hot Carrier Cooling Enables van der Waals Photodetectors at Telecom Wavelengths

Zhouxiaosong Zeng[1,2]†, Yufan Wang[2]†, Patrick Michel[1], Fabian Strauß[1], Xiao Wang[2,3]*, Kai Braun[1]*, Marcus Scheele[1]*

[1]Institute of Physical and Theoretical Chemistry and LISA+, University of Tübingen, Auf der Morgenstelle 18, D-72076, Tübingen, Germany

[2] School of Physics and Electronics, Hunan University, Changsha 410082, China

[3] Key Laboratory for Micro-Nano Physics and Technology of Hunan Province, College of Materials Science and Engineering, Hunan University, Changsha, 410082, China

*Corresponding authors:

E-mail addresses: xiao_wang@hnu.edu.cn(X. Wang); kai.braun@uni-tuebingen.de (K. Braun); marcus.scheele@uni-tuebingen.de (M. Scheele)

Abstract: With the increasing demand for optical data transmission and processing by modern communication systems, high-speed optoelectronics operating at telecom wavelengths are greatly desired. Two-dimensional (2D) materials with high carrier mobility and picosecond intrinsic response times exhibit large potential in this respect. However, most reported 2D material photodetectors for the telecom C-band either suffer from a slow response speed or rely on integrated silicon waveguides, which is a consequence of the inefficient utilization of hot carriers in these devices. Here, we report a high-performance and waveguide-free WS_2/graphene photodetector operating at 1560 nm enabled by hot carrier injection and long-lived charge separation. The

efficiently injected hot electrons from graphene to WS_2 exhibit ultrafast cooling dynamics with 3 ps intrinsic response time. Simultaneous hole trapping in WS_2 ensures a long circulation of injected electrons, enabling a high responsivity of 0.26 A/W. In continuation, we present a vertical WS_2/graphene/WSe_2 device with a built-in electric field and the same detection mechanism, for which a photocurrent on-off ratio of 3500 and an extrinsic response time of 1.71 ns are obtained. Our study highlights the benefits of combing 2D semiconductors and semimetals for high-speed photodetection.

Introduction:

Fast photodetectors that convert an on-chip optical signal into an electrical output at high-speed are vital for modern imaging, sensing, and communication systems[1]. Operation at telecom wavelengths is especially preferred due to low transmission losses and the availability of optical gain. Two-dimensional (2D) transition metal dichalcogenides (TMDCs) with bond-free van der Waals (vdW) structures possess relatively large carrier mobilities[2-4] and intrinsic response times on the order of picoseconds[5-7], demonstrating great potential for the next generation of ultrafast photodetectors.

One of the most important challenges for the development of information technology is the large heat dissipation caused by long-distance data transmission and fast signal conversion in high densities[8]. A major source for such electrical heat is the generation of hot electrons, which refers to high-temperature carriers beyond the thermal equilibrium with the lattice[9]. If this electrical heat could be effectively

harnessed, heat dissipation would be reduced and the power conversion efficiency of the device simultaneously enhanced[10]. A promising strategy in this respect is the photo-thermionic effect. Briefly, if the photon energy of the optical signal is higher than the Schottky barrier between a metal and a semiconductor, the photogenerated hot electrons in the metal can be extracted and injected into the adjacent semiconductor after their thermalization[11]. This photoelectric effect enables a sub-bandgap photoresponse at telecom wavelengths in 2D TMDCs without sacrificing response speed. However, due to the relatively weak light absorption by the metal, the conventional metal-semiconductor-metal structure requires an integration into silicon waveguides to enhance the hot electron injection efficiency[12, 13], which makes the device configuration sophisticated and limits the response to certain wavelengths.

In a related strategy, graphene has been reported as a material for the thermoelectric management of nanoscale devices due to its high thermal conductivity[14], low heat capacity[15], and unique hot carrier cooling dynamics[16, 17]. After excitation, the photogenerated charge carriers in graphene can thermalize themselves via carrier scattering with a temperature of hundreds of Kelvins higher than the lattice, inducing excess electrical heat[16]. With its gapless band structure and vdW property, combining graphene and TMDCs to construct heterostructure devices targets the utilization of these hot electrons for photodetection at telecom wavelengths with highly efficient hot carrier injection, reduced wasted heat, and low dark currents. The charge carrier dynamics in graphene/TMDC heterostructures have been extensively investigated via

all-optical pump-probe methods, where hot carrier transfer or injection from graphene to adjacent layers over the Schottky barrier is reported at the picosecond time scale[18, 19]. Terahertz and all-optical pump-probe studies showed that the injected hot electrons can be trapped by the defects[20] in the TMDC or recycled via electron-phonon interactions[21] from the heterostructure. This way, the injected carrier lifetime could be extended to nanoseconds, which enabled the harvesting of hot carriers over realistic device lengths. This is an important prerequisite for solving the trade-off between high response speed and high responsivity in such a device. However, a demonstration of this principle in actual devices via optical pump-photocurrent probe experiments have not been reported so far.

Here, we construct a waveguide-free WS_2/graphene photodetector and apply the two-pulse coincidence (2PC) photoresponse technique via asynchronous optical sampling (ASOPS) to determine the hot carrier dynamics that contributes to the photocurrent. Upon 1560 nm excitation, the heterostructure photodetector exhibits two lifetime components with $\tau_{fast} \approx 3$ ps and $\tau_{slow} \approx 500$ ps. We attribute the τ_{fast} to a hot carrier injection and cooling, which we rationalize in terms of its super-linear power-dependence, the positive contribution to the photocurrent, and an increasing lifetime with decreasing temperature. We argue that the slow component resembles trapped holes in the TMDC, which is supported by its negative contribution to the photocurrent and its disappearance upon applying large biases. The fast hot carrier cooling and long circulation of electrons in the heterostructure affords a telecom

C-band-suited photodetector with a simultaneously enhanced photoresponse speed and responsivity. Moreover, we show that the photodetection performance can be further increased by designing a vertical WS_2/graphene/WSe_2 device with an out-of-plane built-in electric field and the same hot carrier injection mechanism. For this device, the photocurrent on-off ratio is 3500 with an extrinsic response time of 1.71 ns and a responsivity of 0.18 A/W.

Results:

The WS_2/graphene heterostructure in this study was fabricated via a standard all-dry transfer technique and low-temperature annealing. E-beam lithography (EBL) and thermal evaporation were then employed to define Au/Cr electrodes. Before transferring a WS_2 layer on an exfoliated graphene flake, oxygen plasma treatment was first introduced to etch the graphene into a desired shape. Figure 1a exhibits an optical microscopy image of a typical device, where both electrodes were fabricated on top of thin-layered WS_2. A Raman spectrum (Figure 1b) collected at the heterostructure region indicates the fingerprint of WS_2 (*2LA*(*M*) peak at 351.6)[22] and graphene (*G* peak at 1582 cm^{-1} and *2D* peak at 2700 cm^{-1})[23].

We investigate the photoresponse in the heterostructure device by a scanning photocurrent microscope (SPCM). Under sub-WS_2 bandgap (780 nm) excitation, we find a photocurrent with unchanged polarity at the heterostructure region and detect only a weak signal at the electrode edges (Figure 1c), presumably originating from the hot carriers generated in graphene. This is detailed further in the extracted

photocurrent line profile (Figure 1d), where the normalized photocurrent intensity at the heterostructure center is one order of magnitude higher than that at the electrodes. Upon increasing the excitation power (Figure 1e, sub-WS_2 bandgap excitation), the obtained photocurrent demonstrates a unique superlinear dependence with a fitted power law of $P \sim 1.38$ (black dots and red line). This is in contrast to the conventional saturated absorption with sub-linear power dependence (Supporting Information Section 1), and we interpret this finding with thermal activation of carriers over the Schottky barrier between WS_2 and graphene[11]. In addition, the device exhibits a high responsivity of approximately 9 A/W at 779 nm and 22.6 mW/cm^2 excitation power density (blue squares).

We now investigate the device behavior under 1560 nm excitation. We use two lasers A and B (see methods: ASOPS) with a similar output power of 90 mW. We find a net photocurrent of 30 nA induced by only laser A (the first step in Figure 1f) which increases by 40 nA upon adding the illumination by laser B (the second step in Figure 1f). This result confirms the superlinear behavior also at telecom wavelengths, indicative of hot carrier injection. The I-V characteristics (Figure. 1g) displays a pronounced photocurrent under illumination by both lasers and a dark current roughly eight orders of magnitude smaller than in pure graphene (Supporting Information Section 2).

We investigate the hot carrier dynamics further by two-pulse coincidence (2PC) measurements in vacuum using ASOPS. Briefly, the device is excited by the two pulsed lasers A and B (pump and probe) separated by a delay time Δt. The

corresponding photoresponse collected by the lock-in amplifier is recorded as a function of delay time Δt between the pulses (Figure 1h) and hence the technique is also called photocurrent autocorrelation[24]. In a typical 2PC measurements, when the pump and the probe lasers coincide spatially and temporally, the generation of photocurrent by the probe is suppressed because of the saturation in the ground state, causing a prominent dip at the zero time delay $\Delta t = 0$. With an increase in the delay time, parts of the pump-induced charge carriers relax, and they can be excited again by the probe beam. Hence, one would expect an exponential recovery of photocurrent with the delay time Δt. Our WS_2/graphene heterostructure device exhibits two lifetime components (Figure i) with τ_{fast} = 3 ps (Figure j) and $\tau_{slow} \approx$ 500 ps (Supporting In formation Section 3), indicating the presence of two distinct dynamic processes. The fast component appears as a peak (positive contribution to the photocurrent) and the slow component as a dip (negative contribution).

To understand the provenance of these two components, we first analyze the fast component. By studying its dependence on the external bias and temperature, we test our previous hypothesis from the 2PC experiment that this component originates from cooling of injected hot carriers (Figure 2b and 2c). Varying the external voltage from 0.5 V to 3.5 V has no significant effect on the response time, which argues against a transport-related mechanisms[25], such as charge carrier drift. The negative correlation with temperature, e.g. the observed increase of the lifetime from 3 ps to 5.2 ps while decreasing the temperature from 300 K to 80 K, rules out a recombination-related

process[7]. We argue that this phenomenon is best explained with phonon-mediated cooling, where additional energy is needed to activate phonons at low temperature, which slows the cooling[26, 27]. It should be noted that the energy of the input laser (0.795 eV) is smaller than half the bandgap energy of thin layered WS_2 (~ 0.96 eV). Therefore, two-photon absorption is unlikely to be responsible for the fast component. The results also indicate that the ultrafast hot carrier cooling in pure graphene is preserved in the WS_2/graphene heterostructure, leading to an intrinsic response time comparable to pure graphene[17].

We continue with analyzing the slow component and argue that it is related to carrier trapping, similar to a recent report for WS_2 based on terahertz spectroscopy[20]. In detail, upon illumination by the 1560 nm laser, electrons and holes in graphene are rapidly injected into the adjacent WS_2 layer (Figure 2e i). After that, a fraction of the hot electrons cool in several picoseconds, inducing an ultrafast intrinsic response peak in the 2PC signal (Figure 2e ii, upper panel). Meanwhile, the injected holes are captured by the defects at the surface of WS_2, which not only leads to a relatively long circulation of the electrons, reflected by the slow intrinsic response dip in the 2PC signal (Figure 2e ii, lower plane), but also contributes to a high responsivity of 0.26 A/W (see Supporting Information Section 6 for detailed calculations). In comparison, a device without the slow dip component possesses one order of magnitude lower responsivity under the same measurement condition (Supporting Information Section 7). In addition, upon increasing the external bias, the dip can be almost entirely suppressed (Figure 2a), presumably due to the depopulation of traps.

The dominant ultrafast hot carrier cooling intrinsic response in the WS_2/graphene heterostructure indicates its high potential for high-speed photodetection. In contrast to the intrinsic response time reflecting an inherent carrier dynamics, the extrinsic response of a photodetector includes additional effects of the device geometry (e.g. its RC time) and serves as a measure for the conventional device speed. To this end, we construct a WS_2/graphene photodetector array (Figure 3b) via oxygen plasma etching and all-dry transfer processes (Figure 3a and Supporting Information Section 8) and determine the extrinsic photoresponse using the experimental setup illustrated in Figure 3c. Upon 779 nm pulse illumination (sub-WS_2 bandgap), the device displays a constant response for several cycles as shown in Figure 3d. We exemplarily extract a single pulse response and resolve it on a semi-log scale axis. The 90% to 10% photocurrent decay indicates an extrinsic response time of 7.11 ns (Figure 3e, black curve). Using fast Fourier transformation (FFT), we calculate the electrical bandwidth under the single excitation frequency and obtain a 3-dB bandwidth of approximately 17.7 MHz (Figure 3f), which is comparable to that of state-of-the-art photodetectors[28, 29] for telecom wavelengths.

To further improve the performance of graphene/TMDC heterostructures based on the ultrafast hot carrier extraction and cooling, we fabricate a vertical WS_2/graphene/WSe_2 heterostructure (Figure 4a and 4b). In 2PC measurements (Supporting Information Section 9), the device demonstrates an intrinsic charge

carrier dynamics similar to that in the sample WS_2/graphene heterostructure, indicating the same photo-thermionic detection process. In the corresponding SPCM experiment (Figure 4c) the photocurrent appears at the heterostructure region, proving the contribution of hot carriers from the graphene. The advantage of this new heterostructure is an additional vertical built-in electric field manifesting in the rectifying transport behavior displayed in Figure 4d and an on-off ratio of 3500, much higher than that of the lateral device. Furthermore, we obtain a laser-frequency independent extrinsic response time of approximately 1.71 ns (Figure 4e) and a 3-dB bandwidth of 123.4 MHz (Figure 4f) at 779 nm laser excitation. Thus, the vertical WS_2/graphene/WSe_2 heterostructure synergistically combines the properties of photodetectors with sole hot carrier injection and that of devices with built-in electric field.

Finally, we compare the photodetection performance of our WS_2/graphene heterostructure with other 2D vdW devices operating at telecom wavelengths. Notably, most results are located at the lower right-hand corner, reflecting a trade-off between responsivity and response time. In contrast, our WS_2/graphene heterostructure with ultrafast hot carrier cooling and long electron circulation simultaneously possesses 3 ps intrinsic response time and 0.26 A/W responsivity while the WS_2/graphene/WSe_2 heterostructure exhibits a 1.71 ns extrinsic response time and 0.18 A/W responsivity, which are among one of the best performances (Figure 5).

Conclusion:

In summary, using the two-pulse coincidence photoresponse technique, we present graphene/WS_2 and WS_2/graphene/WSe_2 photodetectors that exhibit clear signs of hot carrier injection from graphene into the van der Waals materials followed by carrier trapping. The injected hot carriers exhibit ultrafast cooling and the carrier trapping induces a long circulation of the electrons, whose combination enables an intrinsic response time of 3 ps and a responsivity of 0.26 A/W at 1560 nm. We demonstrate sub-bandgap photodetection by these heterostructures with a 3dB bandwidth of 123 MHz and a dark current eight orders of magnitude smaller than in pure graphene. Our results highlight that such heterostructures synergistically combine the ultrafast response of graphene with the high sensitivity of transition metal dichalcogenides to harvest hot carriers efficiently.

References

(1) Liu, J.; Xia, F. N.; Xiao, D.; de Abajo, F. J. G.; Sun, D. Semimetals for high-performance photodetection. *Nat. Mater.* **2020**, *19* (8), 830-837.

(2) Ng, H. K.; Xiang, D.; Suwardi, A.; Hu, G. W.; Yang, K.; Zhao, Y. S.; Liu, T.; Cao, Z. H.; Liu, H. J.; Li, S. S.; et al. Improving carrier mobility in two-dimensional semiconductors with rippled materials. *Nat. Electron.* **2022**, *5* (8), 489-496.

(3) Pack, J.; Guo, Y. J.; Liu, Z. Y.; Jessen, B. S.; Holtzman, L.; Liu, S.; Cothrine, M.; Watanabe, K.; Taniguchi, T.; Mandrus, D. G.; et al. Charge-transfer contacts for the measurement of correlated states in high-mobility WSe_2. *Nat. Nanotechnol.* **2024**, *19* (7), 948–954.

(4) Liu, Y.; Guo, J.; Zhu, E. B.; Liao, L.; Lee, S. J.; Ding, M. N.; Shakir, I.; Gambin, V.; Huang, Y.; Duan, X. F. Approaching the Schottky-Mott limit in van der Waals metal-semiconductor junctions. *Nature* **2018**, *557* (7707), 696-700.

(5) Zeng, Z. X. S.; Tian, Z. Q.; Wang, Y. F.; Ge, C. H.; Strauss, F.; Braun, K.; Michel, P.; Huang, L. Y.; Liu, G. X.; Li, D.; et al. Dual polarization-enabled ultrafast bulk photovoltaic response in van der Waals heterostructures. *Nat. Commun.* **2024**, *15* (1), 5355.

(6) Zeng, Z. X. S.; Braun, K.; Ge, C. H.; Eberle, M.; Zhu, C. G.; Sun, X. X.; Yang, X.; Yi, J. L.; Liang, D. L.; Wang, Y. F.; et al. Picosecond electrical response in graphene/$MoTe_2$ heterojunction with high responsivity in the near infrared region. *Fundam. Res.* **2022**, *2* (3), 405-411.

(7) Wang, H. N.; Zhang, C. J.; Chan, W. M.; Tiwari, S.; Rana, F. Ultrafast response of monolayer molybdenum disulfide photodetectors. *Nat. Commun.* **2015**, *6*, 8831.

(8) Miller, D. A. B. Attojoule Optoelectronics for Low-Energy Information Processing and Communications. *J. Lightwave Technol.* **2017**, *35* (3), 346-396.

(9) Paul, K. K.; Kim, J. H.; Lee, Y. H. Hot carrier photovoltaics in van der Waals heterostructures. *Nat. Rev. Phys.* **2021**, *3* (3), 178-192.

(10) Melnick, C.; Kaviany, M. From thermoelectricity to phonoelectricity. *Appl. Phys. Rev.* **2019**, *6* (2).

(11) Massicotte, M.; Schmidt, P.; Vialla, F.; Watanabe, K.; Taniguchi, T.; Tielrooij, K. J.; Koppens, F. H. L. Photo-thermionic effect in vertical graphene heterostructures. *Nat. Commun.* **2016**, *7*, 12174

(12) Li, Z. W.; Hu, S. Q.; Zhang, Q.; Tian, R. J.; Gu, L. P.; Zhu, Y. S.; Yuan, Q. C.; Yi, R. X.; Li, C.; Liu, Y.; et al. Telecom-Band Waveguide-Integrated MoS_2 Photodetector Assisted by Hot Electrons. *ACS Photonics* **2022**, *9* (1), 282-289.

(13) Zhang, Q.; Ji, Y. K.; Hu, S. Q.; Li, Z. W.; Li, C.; Gu, L. P.; Tian, R. J.; Zhang, J. C.; Fang, L.; Zhao, B. J.; et al. High-responsivity MoS_2 hot-electron telecom-band photodetector integrated with microring resonator. *Appl. Phys. Lett.* **2022**, *120* (26), 261111.

(14) Balandin, A. A.; Ghosh, S.; Bao, W. Z.; Calizo, I.; Teweldebrhan, D.; Miao, F.; Lau, C. N. Superior thermal conductivity of single-layer graphene. *Nano Lett.* **2008**, *8* (3), 902-907.

(15) Aamir, M. A.; Moore, J. N.; Lu, X. B.; Seifert, P.; Englund, D.; Fong, K. C.; Efetov, D. K. Ultrasensitive Calorimetric Measurements of the Electronic Heat Capacity of Graphene. *Nano Lett.* **2021**, *21* (12), 5330-5337.

(16) Tielrooij, K. J.; Hesp, N. C. H.; Principi, A.; Lundeberg, M. B.; Pogna, E. A. A.; Banszerus, L.; Mics, Z.; Massicotte, M.; Schmidt, P.; Davydovskaya, D.; et al. Out-of-plane heat transfer in van der Waals stacks through electron-hyperbolic phonon coupling. *Nat. Nanotechnol.* **2018**, *13* (1), 41-46.

(17) Sun, D.; Aivazian, G.; Jones, A. M.; Ross, J. S.; Yao, W.; Cobden, D.; Xu, X. D. Ultrafast hot-carrier-dominated photocurrent in graphene. *Nat. Nanotechnol.* **2012**, *7* (2), 114-118.

(18) Chen, Y. Z.; Li, Y. J.; Zhao, Y. D.; Zhou, H. Z.; Zhu, H. M. Highly efficient hot electron harvesting from graphene before electron-hole thermalization. *Sci. Adv.* **2019**, *5* (11), eaax9958.

(19) Yuan, L.; Chung, T. F.; Kuc, A.; Wan, Y.; Xu, Y.; Chen, Y. P.; Heine, T.; Huang, L. B. Photocarrier generation from interlayer charge-transfer transitions in WS_2-graphene heterostructures. *Sci. Adv.* **2018**, *4* (2), e1700324.

(20) Fu, S.; du Fossé, I.; Jia, X. Y.; Xu, J. Y.; Yu, X. Q.; Zhang, H.; Zheng, W. H.;

Krasel, S.; Chen, Z. P.; Wang, Z. M. M.; et al. Long-lived charge separation following pump-wavelength-dependent ultrafast charge transfer in graphene/WS_2 heterostructures. *Sci. Adv.* **2021**, *7* (9), eabd9061.

(21) Wei, K.; Sui, Y. Z.; Xu, Z. J.; Kang, Y.; You, J.; Tang, Y. X.; Li, H.; Ma, Y. T.; Ouyang, H.; Zheng, X.; et al. Acoustic phonon recycling for photocarrier generation in graphene-WS_2 heterostructures. *Nat. Commun.* **2020**, *11* (1), 3876.

(22) Zeng, H. L.; Liu, G. B.; Dai, J. F.; Yan, Y. J.; Zhu, B. R.; He, R. C.; Xie, L.; Xu, S. J.; Chen, X. H.; Yao, W.; et al. Optical signature of symmetry variations and spin-valley coupling in atomically thin tungsten dichalcogenides. *Sci. Rep.* **2013**, *3*, 1608.

(23) Ferrari, A. C.; Basko, D. M. Raman spectroscopy as a versatile tool for studying the properties of graphene. *Nat. Nanotechnol.* **2013**, *8* (4), 235-246.

(24) Maier, A.; Strauss, F.; Kohlschreiber, P.; Schedel, C.; Braun, K.; Scheele, M. Sub-nanosecond Intrinsic Response Time of PbS Nanocrystal IR-Photodetectors. *Nano Lett.* **2022**, *22* (7), 2809-2816.

(25) Massicotte, M.; Schmidt, P.; Vialla, F.; Schädler, K. G.; Reserbat-Plantey, A.; Watanabe, K.; Taniguchi, T.; Tielrooij, K. J.; Koppens, F. H. L. Picosecond photoresponse in van der Waals heterostructures. *Nat. Nanotechnol.* **2016**, *11* (1), 42-46.

(26) Menabde, S. G.; Cho, H.; Park, N. Interface defect-assisted phonon scattering of hot carriers in graphene. *Phys. Rev. B* **2017**, *96* (7), 075426.

(27) Graham, M. W.; Shi, S. F.; Ralph, D. C.; Park, J.; McEuen, P. L. Photocurrent measurements of supercollision cooling in graphene. *Nat. Phys.* **2013**, *9* (2), 103-108.

(28) Rogalski, A. Infrared detectors: status and trends. *Prog. Quantum Electron.* **2003**, *27* (2), 59-210.

(29) Rogalski, A. Progress in focal plane array technologies. *Prog. Quantum Electron.* **2012**, *36* (2), 342-473.

(30) Wang, Y.; Yu, Z. J.; Tong, Y. Y.; Sun, B. L.; Zhang, Z. Y.; Xu, J. B.; Sun, X. K.; Tsang, H. K. High-speed infrared two-dimensional platinum diselenide photodetectors. *Appl. Phys. Lett.* **2020**, *116* (21), 211101.

(31) Tian, R. J.; Gan, X. T.; Li, C.; Chen, X. Q.; Hu, S. Q.; Gu, L. P.; Van Thourhout, D.; Castellanos-Gomez, A.; Sun, Z. P.; Zhao, J. L. Chip-integrated van der Waals PN heterojunction photodetector with low dark current and high responsivity. *Light-Sci. Appl.* **2022**, *11* (1), 101.

(32) Maiti, R.; Patil, C.; Saadi, M.; Xie, T.; Azadani, J. G.; Uluutku, B.; Amin, R.; Briggs, A. F.; Miscuglio, M.; Van Thourhout, D.; et al. Strain-engineered high-responsivity $MoTe_2$ photodetector for silicon photonic integrated circuits. *Nat. Photonics* **2020**, *14* (9), 578-584.

(33) Wang, L.; Li, J. J.; Fan, Q.; Huang, Z. F.; Lu, Y. C.; Xie, C.; Wu, C. Y.; Luo, L. B. A high-performance near-infrared light photovoltaic detector based on a multilayered $PtSe_2$/Ge heterojunction. *J. Mater. Chem. C* **2019**, *7* (17), 5019-5027.

(34) Xiao, P.; Mao, J.; Ding, K.; Luo, W. J.; Hu, W. D.; Zhang, X. J.; Zhang, X. H.; Jie, J. S. Solution-Processed 3D RGO-MoS_2/Pyramid Si Heterojunction for Ultrahigh Detectivity and Ultra-Broadband Photodetection. *Adv. Mater.* **2018**, *30* (31), 1801729.

(35) Ye, L.; Li, H.; Chen, Z. F.; Xu, J. B. Near-Infrared Photodetector Based on MoS2/Black Phosphorus Heterojunction. *ACS Photonics* **2016**, *3* (4), 692-699.

(36) Wu, D.; Guo, J. W.; Wang, C. Q.; Ren, X. Y.; Chen, Y. S.; Lin, P.; Zeng, L. H.; Shi, Z. F.; Li, X. J.; Shan, C. X.; et al. Ultrabroadband and High-Detectivity Photodetector Based on WS_2/Ge Heterojunction through Defect Engineering and Interface Passivation. *ACS Nano* **2021**, *15* (6), 10119-10129.

(37) Luo, L. B.; Wang, D.; Xie, C.; Hu, J. G.; Zhao, X. Y.; Liang, F. X. $PdSe_2$ Multilayer on Germanium Nanocones Array with Light Trapping Effect for Sensitive Infrared Photodetector and Image Sensing Application. *Adv. Funct. Mater.* **2019**, *29* (22), 1900849.

(38) Hong, C.; Oh, S.; Dat, V. K.; Pak, S.; Cha, S. N.; Ko, K. H.; Choi, G. M.; Low, T.; Oh, S. H.; Kim, J. H. Engineering electrode interfaces for telecom-band photodetection in MoS_2/Au heterostructures via sub-band light absorption. *Light-Sci. Appl.* **2023**, *12* (1), 280.

(39) Yu, Y. F.; Sun, Y.; Hu, Z. L.; An, X. H.; Zhou, D. M.; Zhou, H. Z.; Wang, W. H.; Liu, K. Y.; Jiang, J.; Yang, D. D.; et al. Fast Photoelectric Conversion in the

Near-Infrared Enabled by Plasmon-Induced Hot-Electron Transfer. *Adv. Mater.* **2019**, *31* (43), 1903829.

(40) Qiao, H.; Yuan, J.; Xu, Z. Q.; Chen, C. Y.; Lin, S. H.; Wang, Y. S.; Song, J. C.; Liu, Y.; Khan, Q.; Hoh, H. Y.; et al. Broadband Photodetectors Based on Graphene-Bi_2Te_3 Heterostructure. *ACS Nano* **2015**, *9* (2), 1886-1894.

(41) Shu, X. R.; Wu, J. F.; Zhong, F.; Zhang, X. L.; Fu, Q.; Han, X.; Zhang, J. L.; Lu, J. P.; Ni, Z. H. High-responsivity, high-detectivity, broadband infrared photodetector based on MoS_2/BP/MoS_2 junction field-effect transistor. *Appl. Phys. Lett.* **2024**, *124* (18), 181101.

(42) Kang, X. L.; Lan, C. Y.; Li, F. Z.; Wang, W.; Yip, S.; Meng, Y.; Wang, F.; Lai, Z. X.; Liu, C. T.; Ho, J. C. Van der Waals $PdSe_2$/WS_2 Heterostructures for Robust High-Performance Broadband Photodetection from Visible to Infrared Optical Communication Band. *Adv. Opt. Mater.* **2021**, *9* (7), 2001991.

Author Contributions:

Z. Z., and Y. W. contributed equally to this work. Z. Z., K. B., and M. S. conceived the original project. Y. W. fabricated the devices and carried out SPCM measurements. Z. Z., F. S., and P. M. carried out the extrinsic photoresponse measurements. Z. Z. carried out the 2PC measurements with the input of P. M. Z. Z. performed data analysis. Z. Z., X. W. and M. S. wrote the manuscript. X. W., K. B., and M. S. supervised the work. All authors contributed to the general discussion.

Acknowledgements:

Z. Z. acknowledges the Alexander von Humboldt foundation for a postdoctoral fellowship. Financial support of this work has been provided by the Deutsche Forschungsgemeinschaft (DFG) under grant SCHE1905/9-1 (project no. 426008387), the by the European Research Council (ERC) under the European Union's Horizon 2020 research and innovation program (grant agreement No 802822), the National Natural Science Foundation of China (Nos. U23A20570, 52302175, 52221001, 92263107), and the Hunan Provincial Natural Science Foundation of China (No. 2023JJ40138), and the science and technology innovation Program of Hunan Province (Nos. 2024RC1034 and 2020XK2001).

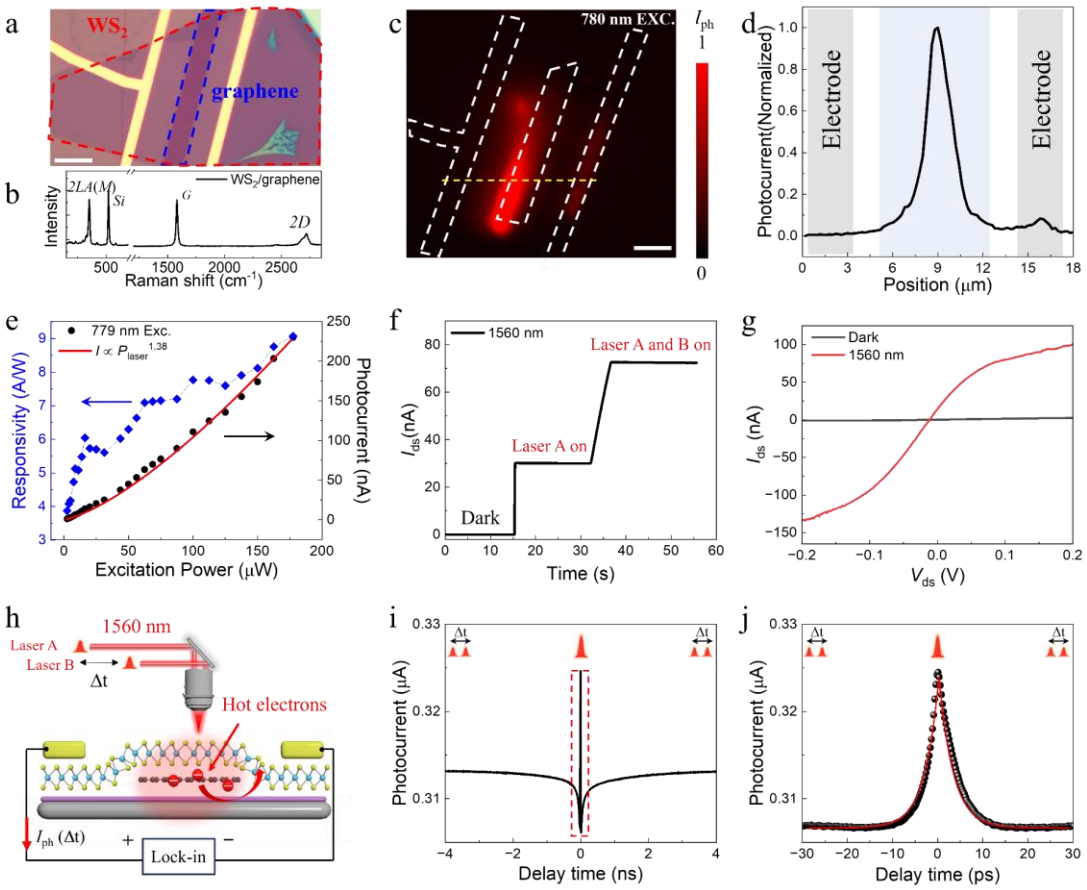

Figure 1. Hot carrier injection enabled WS_2/graphene photodetector. (a) Optical image of a WS_2/graphene photodetector, where the red and blue dashed lines highlight the WS_2 and graphene layers, respectively. The scale bar is 10 μm. (b) Raman spectrum of the heterostructure. (c) Scanning photocurrent microscopy showing the spatially-resolved photoresponse under sub-WS_2 bandgap excitation, where the dashed white lines indicate the positions of electrodes and the heterostructure overlayer. The color bar represents the normalized photocurrent intensity. The scale bar is 7 μm. (d) Extracted photocurrent line profile along the dashed yellow line in c. The light blue area indicates the position of the heterostructure. (e) Excitation power density dependence of responsivity (left) and photocurrent (right) under 779 nm (sub-WS_2 bandgap) excitation. The red line is a power-law fit with $I_{pc} \approx P^{1.38}$. (f) Time-resolved photoresponse under 1560 nm excitation. Both, laser A and laser B, have a similar output power of approximately 90 mW. (g) I-V characteristic curves in

dark (black) and under 1560 nm illumination (red). The small short-circuit current could originate from the unbalanced illumination from a laser fiber. (h) Schematic illustration of two-pulse coincidence (2PC) measurement with 1560 nm excitation. (i) 2PC measurement under a bias of 0.3 V, where the change in photocurrent ΔP induced by the probe laser is plotted as a function of delay time Δt. (j) Zoomed-in 2PC measurement result corresponding to the red rectangle region in i.

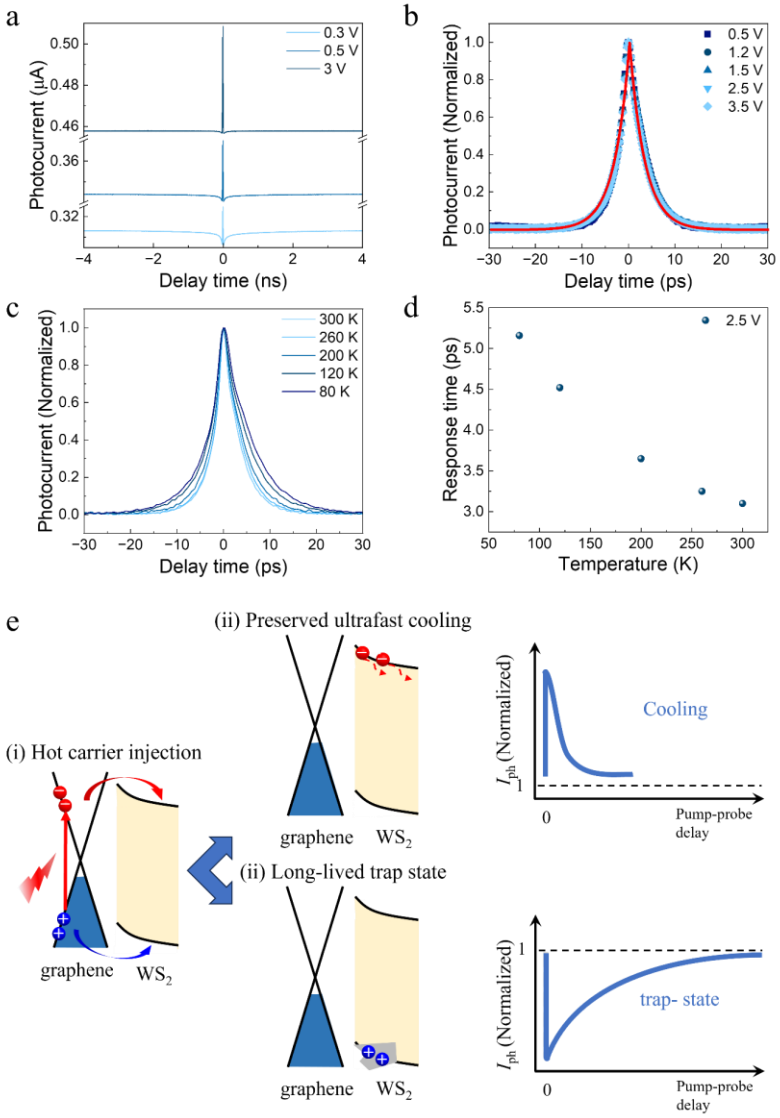

Figure 2. Two-pulse coincidence (2PC) measurements of a WS_2/graphene photodetector. (a) External voltage dependence of the 2PC results. (b) External voltage dependence of the 2PC results for time delay from -30 ps to 30 ps. (c) Temperature dependence of 2PC results for time delay from -30 ps to 30 ps. (d) Corresponding temperature-dependent intrinsic response times. (e) Schematical illustration of hot carrier dynamics in WS_2/graphene. Upon illumination, the generated electrons and holes in graphene are injected into WS_2 (i). The injected hot electrons possess ultrafast cooling similar to that of pure graphene and demonstrate a fast peak signal in 2PC measurement (ii, upper plane); While the injected holes are trapped by the surface defects at the WS_2 and contribute to a long circulation of

injected electrons, which demonstrate a slow dip signal in 2PC measurement (ii, lower plane).

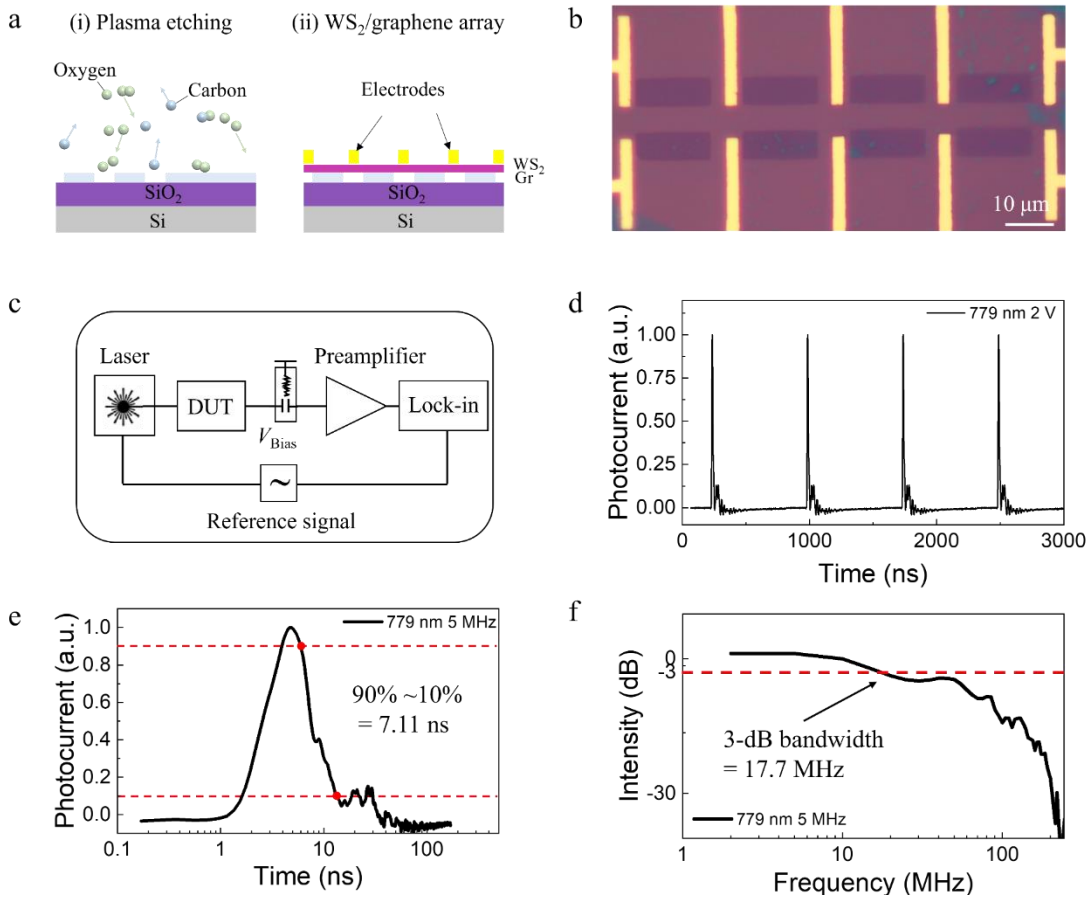

Figure 3. Extrinsic and 3-dB bandwidth of a WS_2/graphene photodetector array. (a) Schematic illustration of the array fabrication processes. (b) Optical image of a WS_2/graphene photodetector array. (c) Experimental configuration for the extrinsic response time measurements. DUT, device under test. (d) Photoresponse towards a 779 nm (sub-WS_2 excitation) pulse sequence under 2 V external voltage. (e) Normalized extrinsic response in semi-log scale towards a 779 nm laser with 5 MHz repetition frequency. The extrinsic response time defined by the 90% to 10% photocurrent decay (indicated by the red dots and the dashed line). (f) Fourier transformed 3-dB bandwidth corresponding to the result in e.

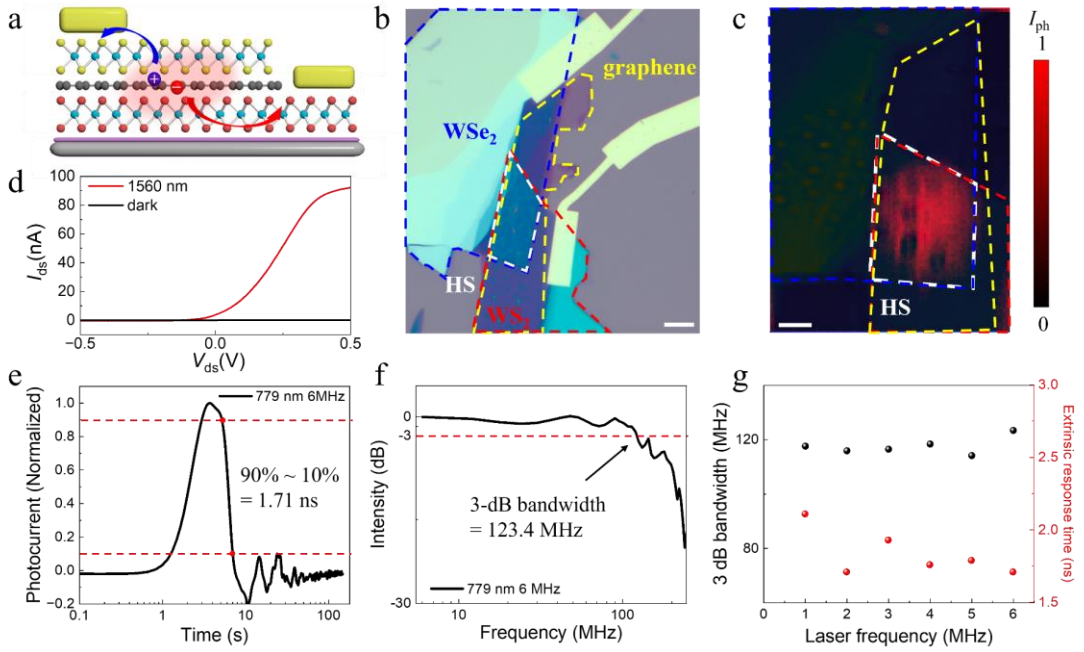

Figure 4. Photodetection of a WS_2/graphene/WSe_2 device with synergistic hot carrier injection and built-in electric field. (a) Schematics of the device. (b) Optical image, where the top electrode and bottom electrode were fabricated on WS_2 and WSe_2 layers, respectively. The scale bar is 7 μm. (c) Superimposed corresponding reflective image and SPCM result under 780 nm illumination, where the dashed blue, yellow, red, and white lines indicate the positions of WSe_2, graphene, WS_2, and heterostructure overlayer, respectively. The color bar represents the normalized photocurrent intensity. The scale bar is 3 μm. (d) I-V characteristic curve in dark (black) and under 1560 nm illumination. (e) Normalized extrinsic response in semi-log scale towards a 779 nm laser with 6 MHz repetition frequency. (f) Corresponding 3-dB bandwidth obtained by Fourier transformation. (g) 779 nm laser frequency dependence of the extrinsic response time (red) and the 3-dB bandwidth (black).

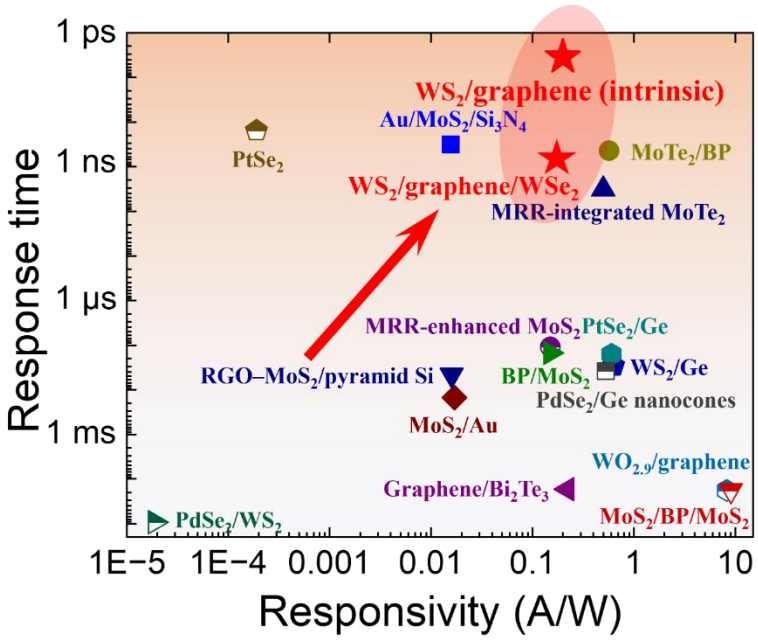

Figure 5. Overview of response time and responsivity in various vdW photodetectors operating at telecom wavelengths. Data for other devices are taken from the literature. ($Au/MoS_2/Si_3N_4$, ref.[12]; $PtSe_2$, ref.[30]; $MoTe_2/BP$, ref.[31]; microring resonators (MRR)-integrated $MoTe_2$, ref.[32]; MRR-enhanced MoS_2, ref.[13]; $PtSe_2/Ge$, ref.[33]; RGO-MoS_2/pyramid Si, ref.[34]; BP/MoS_2, ref.[35]; WS_2/Ge, ref.[36]; $PdSe_2$/Ge nanocones, ref.[37]; MoS_2/Au, ref.[38]; $WO_{2.9}$/graphene, ref.[39]; Graphene/Bi_2Te_3, ref.[40]; $MoS_2/BP/MoS_2$, ref.[41]; $PdSe_2/WS_2$, ref.[42])